

# Magnetohydrodynamic Drive for Water-Based CubeSat Propulsion

Macià Monfort-Castillo\* and Álvaro Romero-Calvo†

*Georgia Institute of Technology, Atlanta, Georgia, 30332, United States of America*

**An analytical model is developed to estimate the performance of a novel low-gravity magnetohydrodynamic (MHD) electrolytic cell architecture. This technology is currently under development with the ultimate goal of separating hydrogen and oxygen from water in microgravity. The model employs the balance of moments between the Lorentz force and the shear stress exerted by the velocity difference of the fluid near the walls. Preliminary analytical results predict the angular velocity of the water-electrolyte depending on the geometry, the magnetic field, and the voltage between electrodes. After computing the angular velocity, the model computes the centripetal acceleration exerted into the liquid. This acceleration is used to derive the radial terminal velocity of gas bubbles and determine the extraction capacity of the device. Ultimately, these tools enable a preliminary analysis and optimization of the system, which with a 1U size and a mass of 0.15kg produces 0.3884 mL/s of hydrogen and 0.1942ml/s of oxygen.**

## I. Introduction

CUBE<sub>SAT</sub> are a class of nanosatellites that are built to standard dimensions of a 10 cm cube (or “Unit”) with a mass of up to 1.33 kg [1]. CubeSats are nowadays extremely popular and their applications have evolved from education to scientific research and industry. They are put into orbit by deployers on the International Space Station or as secondary payloads on a launch vehicle. Nevertheless, most of them are launched by Universities and Institutes [2] to carry out cost-effective scientific studies and technology demonstrations. Missions performed by CubeSats range from remote sensing [3], to research and development [4] passing through biology [5] and interplanetary exploration [6].

Although by 2010, only eight propelled pico- and nanosatellites had been launched [2], the tendency has drastically changed, and novel propelled CubeSats are being designed for future missions. Only in the Artemis 1 launch, four propelled CubeSats were included [7, 8]. The growing interest in propelled CubeSats is fueled by the highly demanding capabilities required to accomplish the science and engineering objectives of new missions.

The nature of the rideshare proposition and the proximity of multiple unrelated CubeSat units constrains CubeSat propulsion architectures. To minimize the risk of critical failures across the board, traditional high-performance fuels, which require pressure vessels and represent a safety hazard, are not a viable option [9, 10]. The explored alternatives include cold gas [11, 12] and electric [13, 14] propulsion or solar sails [15].

Water has been proposed as an alternative propellant due to its inherent safety [16]. The explored water propulsion systems are PEM electrolysis [17], electrothermal (resistojets [18], arcjets [19]), electrostatic gridded ion engines [20], electromagnetic (ELF thrusters [21], Hall effect thrusters [22]), and solar thermal [23]. The approach for water-based propulsion explored in this paper is alkaline electrolysis. This strategy involves storing hydrogen and oxygen as water and separating them through electrolysis as needed. This provides the high specific impulse (over 400 s) that is commonly associated with cryogenic hydrogen and oxygen [24]. However, electrolysis of water is faced with the challenges of inducing phase separation in microgravity. The lack of gravitational forces makes phase separation difficult to achieve in space applications. Several approaches have been developed to address this challenge, including centrifuges [25], forced vortical flows [26], inertial [8], membranes [27], and surface-tension-based technologies [28]. A potential solution for this problem is the inertial phase separation method explored in the Cornell University Cislunar Explorer CubeSat [8], which was planned to be launched with Artemis 1. The design induces centripetal gas separation by adopting a spin-stabilized attitude control strategy. However, this also imposes significant constraints on the mission architecture.

Alternatively, a magnetohydrodynamic (MHD) electrolysis approach may be used to separate hydrogen and oxygen from water while enabling a 3-axis attitude control strategy [29, 30]. Lorentz forces induced by a combination of

---

\*Undergraduate Researcher, Daniel Guggenheim School of Aerospace Engineering, Georgia Institute of Technology, AIAA membership number 1421734 maciraf@gmail.com

†Assistant Professor, Daniel Guggenheim School of Aerospace Engineering, Georgia Institute of Technology, acalvo9@gatech.edu

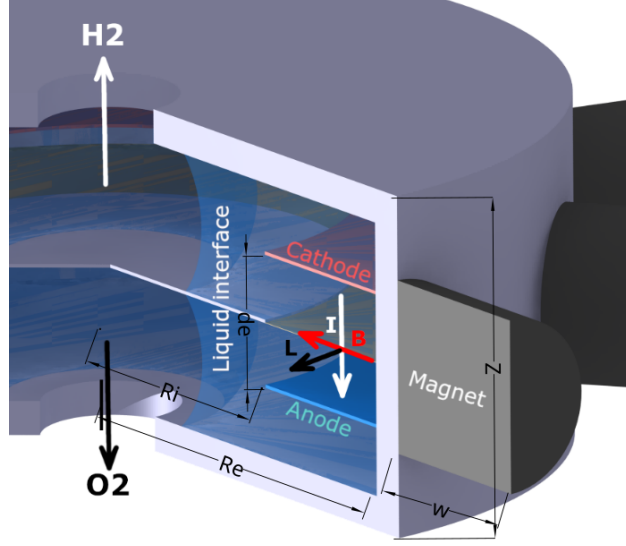


**Fig. 1 Sketch of cylindrical MHD drive for CubeSat.**

electric currents across the electrolyte and an imposed magnetic field are leveraged in a cylindrical cell to induce a rotational movement in the fluid, which acts as a vortical phase separator.

The proposed design is composed of a cylindrical tank filled with a water-electrolyte and gas and subject to an inhomogeneous, axisymmetric, and static magnetic field that varies mainly in the radial direction. The electrolyte is also exposed to an electrical current transmitted between two electrodes, which creates a Lorentz force on the water-electrolyte when subject to the influence of the magnetic field. When the electrolysis process starts, a Lorentz force is applied to the water-electrolyte initiating a rotational movement that separates gas and liquid as if it was a vortical phase separator. This new architecture, depicted in Fig. 1, holds the promise of simplifying water electrolysis systems for space applications by replacing moving parts with simpler magnetohydrodynamic actuators.

Along this paper, Sec. II derives an analytical model of the angular rotation speed, gas production, and gas extraction capability based on the momentum balance. Sec. III presents preliminary results for these metrics and discusses the influence of the MHD drive size, potential difference, magnet size, and electrode distance. Finally, Sec. III concludes with a proposed design for CubeSats application that optimizes the design parameters to increase gas production.

## II. Methods

### A. Simplifying Assumptions

It is assumed that the effect of the gas-liquid interface is negligible. Further, it is assumed that the water-electrolyte is rotating as a solid rigid body except in the boundary layer. This simplification allows us to treat the fluid as a single entity. The approximation of fluid rotating as a solid cylinder is commonly used in the modeling of cylinder swirl in Internal Combustion Engines. This method is named the paddle wheel model, where the volume within the cylinder is idealized to contain an imaginary paddle wheel without mass. As the paddle wheel rotates, the fluid between the blades follows suit, resulting in a cylinder of fluid rotating at a constant angular velocity [31]. This greatly simplifies the mathematical modeling of the system, while still allowing us to capture the essential features of the fluid dynamics.

Moreover, it is assumed that the system is in a steady state. This means that the fluid properties are assumed to be constant in time and that there are no transient effects or fluctuations that would affect the results. It is also assumed that the Blasius conditions [32] hold for the study. The Blasius conditions are typically used to describe a laminar boundary layer that forms on a semi-infinite plate held parallel to a constant unidirectional flow. While these conditions may not be completely accurate for the case under analysis, the rotating flow is assumed to be parallel to the cylindrical walls along  $\theta$ , this still provides a useful approximation that allows simplifying the mathematical modeling of the system.

Finally, the effect that bubbles may have on ion transport and the Lorentz force is neglected, this likely leads to a slightly overestimated current intensity and Lorentz force, however it is essential to develop the model.

## B. Angular Velocity

### 1. Balance of Moments

The shear stress generated by the liquid electrolyte determines the steady-state rotation speed of the MHD drive, thus, the developed approach supposes that to ensure momentum conservation, the sum of the moments exerted by the shear stress in the walls and the moment generated by the Lorentz force must be equal and opposite.

$$M_{\text{shear}} = M_{\text{Lorentz}} \quad (1)$$

### 2. Shear Moment

The moment exerted by the surfaces of the device can be found by integrating the product of the shear stress and the radius,  $\tau(r) \cdot r$ , over the circular surface of the MHD device.

$$M_{\text{shear}} = \iint_S \tau(r) \cdot r \, dr \, d\theta. \quad (2)$$

The shear stress [33] can be expressed as  $\tau = \mu du/dy$ , where  $du/dy$  is the rate of change of the local fluid velocity  $u$  in the normal direction to the shearing surfaces  $y$ , and  $\mu$  is the dynamic viscosity. For the MHD drive analytical approach, it is more convenient to express this equation depending on the angular velocity  $\omega$ , which results in

$$\tau = \mu r \frac{d\omega}{dy}. \quad (3)$$

After assuming a rotation profile of the form  $\omega(y)$  a first-order approximation is done. Any derivative can be roughly estimated as  $dx/dy = (x(y_2) - x(y_1))/(y_2 - y_1)$ , especially for really close  $y_1$  and  $y_2$  values or for a linear variation of  $x$  with  $y$ . For the shear stress in the MHD drive, both cases are true, the variation of the shear stress in a laminar flow is linear, and the boundary layer thickness for the CubeSat-sized MHD drive is small-scaled. Thus, a first-order approximation is used to estimate the shear stress.

The no-slip condition [34] dictates that the speed of the fluid at the boundary (relative to the boundary) is zero; although at some height from the boundary the flow speed must equal that of the fluid. Thus,  $d\omega$  in Eq. 3 can be approximated as the difference between the angular velocity of liquid spinning as a solid rigid body away from the wall ( $\omega_{\text{sr}}$ ) and the angular velocity at the wall (0). Moreover,  $dy$  can be substituted in Eq. 3 by the boundary layer thickness expression  $\delta$ , Eq. 5, which is the distance between a point with angular velocity 0 and a point with an angular velocity equal to  $0.99\omega_{\text{sr}}$ . This first-order simplification results in

$$\tau(r) = \mu r \frac{\omega_{\text{sr}} - 0}{\delta(r)}. \quad (4)$$

It is important to note that the angular velocity is supposed to be constant, while the linear velocity is not. The liquid farther from the center experiences a higher linear velocity, leading to higher shear stress. Conversely, the liquid closer to the center experiences a lower linear velocity, resulting in lower shear stress.

The boundary layer thickness for fluid in the Blasius conditions, given in Sec. II.A, is very closely approximated by

$$\delta = \frac{5}{\sqrt{\text{Re}_x}} x. \quad (5)$$

This expression is dependent on the Reynolds number,  $\text{Re}$ , and the characteristic length  $x$ . For this particular problem, the characteristic length  $x$  is defined as the volume of the system divided by its surface [35],  $x = V_{\text{body}}/A_{\text{surface}}$ .

This variation of linear velocity also affects the thickness of the boundary layer, which is dependent on the linear velocity. Substituting the linear velocity expression  $u = \omega_{\text{sr}} r$  in the boundary layer thickness  $\delta$  (Eq. 5) as  $\text{Re}_x = (\omega_{\text{sr}} r)x/\nu$ , and then, the obtained boundary layer ( $\delta = 5\sqrt{(x \cdot \nu)/(\omega_{\text{sr}} \cdot r)}$ ) in Eq. 4, the shear stress results in

$$\tau(r) = \frac{\mu \omega_{\text{sr}}^{3/2} r^{3/2}}{5\sqrt{x\nu}}. \quad (6)$$

Substituting the expression for the shear stress Eq. 6, and integrating in Eq. 2, the integral results in

$$M_{\text{shear}} = \left[ \frac{4\pi\mu\omega_{\text{sr}}^{3/2} r^{9/2}}{45\sqrt{x\nu}} \right]_{r_1}^{r_2}. \quad (7)$$

### 3. Lorentz Momentum

The magnetic Lorentz force term induced by a magnetic field  $\mathbf{B}$  on a carrying a current  $\mathbf{J}_e$  can be expressed as [36]

$$\mathbf{f}_L = \mathbf{J}_e \times \mathbf{B}, \quad (8)$$

where the electric terms have been neglected due to the consideration of a neutral medium. Considering only the terms in  $\theta$  direction,  $f_{L,\theta} = J_z B_r - J_r B_z$ , where the  $J_r B_z$  value is neglected due to the architecture of the MHD drive. Thus, the Lorentz Force results in

$$F_{\text{Lorentz}} = \int_V J_z B_r dV. \quad (9)$$

The moment exerted by the Lorentz force can be expressed as the product of the applied force and the distance to the center of the drive. The moment exerted by the Lorentz force is

$$M_{\text{Lorentz}} = \int_{z_1}^{z_2} \int_0^{2\pi} \int_{R_i}^{R_e} r J_z B_r(r, z) dz d\theta dr \quad (10)$$

with  $B_r$  being the radial magnetic field (T), and  $J_z$  being the current density ( $A/m^2$ ).

## C. Gas Production

### 1. Water Electrolysis

Water electrolysis process can be understood as decomposition of water into oxygen and hydrogen,



if the electrons pushed through water are known (from current intensity) then, the mol of gas generated per unit of time  $n_{O_2}$  and  $n_{H_2}$  can be obtained, as well as the gas volume production rate

$$V_{\text{gas}} = \frac{(n_{O_2} + n_{H_2})RT}{P}. \quad (12)$$

### 2. Electrolyte Conductivity

For electrochemical water splitting reaction, the thermodynamic potential is 1.23V at 25 °C and 1 atm, though at that voltage external heat is also required. Under practical conditions, approximately 1.5 volts are required.

The current intensity is determined by Ohm's Law  $I = \frac{\Delta V}{R}$  with  $\Delta V$  being the potential difference and  $R$  being the resistance. The potential difference in water electrolysis is limited by the maximum electrode potential of the used electrolyte ( $NaOH$  or  $KOH$  for PEM electrolysis). The standard electrode potential at 298.15K for  $KOH \rightarrow K(c)/OH^-$  is -2.909 V and for  $NaOH \rightarrow Na(c)/OH^-$  is -2.704V [37].

The resistance,  $R$ , is proportional to the distance between the electrodes  $d_e$  and is inversely proportional to the cross-sectional area of the sample,  $A$ . Writing  $\kappa_c$  for the specific conductance (conductivity), the resistance results in  $R = d_e / (A\kappa_c)$ . The experimentally observed  $\kappa_c$  for a 1M  $HClO_4$  + 1% isoprophyl alcohol (IPA) is  $7.29 \pm 0.65$  S/m, which is the value used for the analysis. Now, an expression for the current intensity  $I$  can be obtained from the distance between electrodes,  $d_e$ , the electrode area,  $A$ , the conductivity of the electrolyte  $\kappa_c$  and the potential differential  $\Delta V$ .

$$I = \frac{\Delta V A \kappa_c}{d_e}. \quad (13)$$

## D. Extraction Capacity

The terminal speed of a bubble in a fluid can be determined by analyzing the balance between the drag and buoyancy forces. This is valid for a fluid in a steady state and a bubble moving at its terminal velocity. This balance allows isolating the terminal velocity as [38]

$$u_t = \sqrt{\frac{4g(\rho_L - \rho_G)d_b}{3C_D\rho_L}}, \quad (14)$$

with  $\rho_L, \rho_G$  being the density of the liquid and the gas respectively,  $g$  being the gravity,  $d_b$  being the diameter of the bubble,  $C_D$  being the drag coefficient for the bubble and  $u_t$  being the terminal velocity.

The gravitational force applied to the MHD device corresponds to the normal acceleration, which is the acceleration in the radial direction due to the fluid's rotation. This can be represented as  $g = a_n = \omega_{sr}^2 r$ . This expression for  $u_t$  depends on the drag coefficient  $C_D$  and diameter of the bubble  $d_b$  which are unknown. For the drag coefficient, there is a correlation provided by Rumpf that is valid for Reynolds numbers in the range  $[0.01, 100]$ ,  $C_D = \kappa + 24/Re$ , with  $\kappa = 2$  for  $Re \in [0.01, 10]$  ( $\pm 5\%$  error) and  $\kappa = 1$  for  $Re \in [10, 100]$  ( $\pm 20\%$  error) [39]. This  $C_D$  correlation can be substituted in Eq. 14 using  $Re = u_t d_b \rho_L / \mu_L$ . This particular formulation simplifies the derivation of the analytical closed-form result

$$u_t = \frac{-36\mu_L + 2\sqrt{324\mu_L^2 + 3d_e^3\rho_L\kappa r\omega_{sr}^2(-\rho_g + \rho_L)}}{3d_e\rho_L\kappa}. \quad (15)$$

The produced gas is properly extracted if a stable liquid-gas interface radius is obtained. To maintain a stable liquid-gas interface radius, the bubble flow rate  $Q$  at the interface must be equal to the gas produced in the electrolysis process. The flow rate at a given radius can be calculated supposing a limit condition where the cylindrical interface surface is covered by bubbles. Thus, the bubble flow rate is depend on the terminal velocity of the bubble and on the given surface as,  $Q = S(r, H) \cdot u_t(\omega_{sr}, r)$ . With the surface being  $S = (2\pi r)H$ , and the terminal velocity for the bubbles being  $u_t$  Eq. 15 depending on the radius. By equating the rate of gas production and the rate of gas extraction, the desired stable liquid-gas interface radius is obtained

$$Q_{\text{produced}}(I) = S(r, H) \cdot u_t(\omega_{sr}, r). \quad (16)$$

It must be taken into account that the  $H$  term is first equal to the electrode distance  $d_e$ , as the gas is produced in the space between electrodes and it must be first evacuated from this space. If the calculated interface radius  $R_{\text{interface}}$  using  $H = d_e$  is higher than the electrode internal radius  $R_i$ , some surface of the electrodes is covered by gas, stopping the electrolysis process. On the other hand, if  $R_{\text{interface}} < R_i$ , the gas is evacuated properly from the space between electrodes and the interface radius can be recalculated using  $H = Z$  which leads to a much lower equilibrium radius. Thus, there is a critical point if the gas cannot be evacuated from the space between electrodes, which provokes the electrolysis process to stop.

## E. Magnetic Field

The magnetic field generated by the permanent magnet is computed as the superposition of that induced by  $N = 20$  equivalent circular loops located at the top and bottom walls. Each loop has a current  $I_{\text{loop}} = M_r(R_{\text{magnet e}} - R_{\text{magnet i}})/N$ , resulting in an analogous magnetic system with an analytical solution. Further details on the virtual magnet substitution method can be found in Ref. 40.

# III. Results and Discussion

## A. Angular Rotation Velocity

The match of the moment generated by the shear stress in the different surfaces and the moment exerted by the Lorentz force Eq. 10 results in an equation where the only unknowns for a given geometry and magnetic field are the intensity  $I$  and the rotation velocity  $\omega_{sr}$ . Isolating the angular velocity term  $\omega_{sr}$  an expression for the angular velocity in terms of the Lorentz Force is obtained. The model predicts that  $\omega_{sr} \propto F_{\text{Lorentz}}^{2/3}$ .

From the analytical solution of the magnetic field, it can be observed that it is dependent on the distance to the magnet as shown in Fig. 2(b). From this magnetic field result, a volumetric integral can be computed for the volume between electrodes using Eq. 10. For a particular geometry of  $R_e = 2.3\text{cm}$ ,  $R_i = 1.5\text{cm}$ ,  $d_e = 1\text{cm}$ ,  $Z = 1.905\text{cm}$ ,  $w_{\text{mag}} = 3.175\text{mm}$  and the magnetic field generated by a magnet of this thickness, Fig. 2(b), the predicted  $\omega_{sr}$  variation with the intensity is shown in Fig. 2(a).

## B. Extraction Capacity

To determine the validity of the terminal velocity expression of the buoyancy-drag balance Eq. 15, the Reynolds number is analyzed for different bubble diameters.

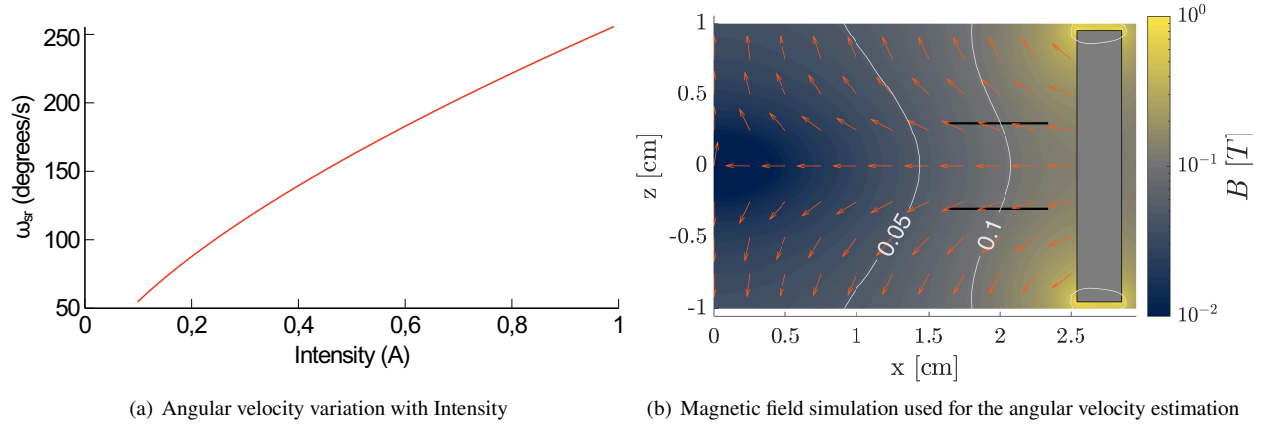


**Fig. 2 Angular velocity variation with Intensity for the shown magnetic field with X dimensions.**

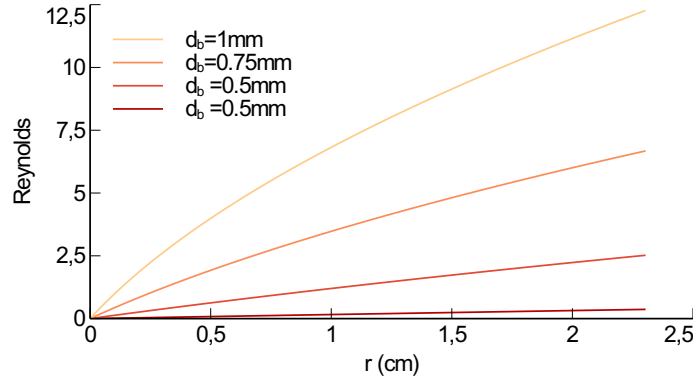


**Fig. 3 Radial velocity along the radius for the intensity of 1 A, with different bubble diameters for Drag-Buoyancy balance.**

Let us use the calculated angular velocity in Fig. 2 for  $I = 1A$  in Eq. 15. Then, the Reynolds number is plotted for various bubble radii in Fig. 3. The bubble diameter influences the Reynolds number in two ways: a larger diameter leads to a higher radial velocity and a larger characteristic length, both of which result in a higher Reynolds number.

It can be noted from the results of the Reynolds number plotted in Fig. 3, that all the bubbles fall within the range of  $Re \in [0.01, 10]$ . Thus, it can be derived that the Rumpf correlation for the drag coefficient is applicable.

### C. Parametric Analysis

In order to design an optimized architecture for the device, a parametric analysis is conducted to examine the impact of several key factors on its performance. Specifically, the study explores the effect of varying the external radius of the device ( $R_e$ ), the applied voltage difference ( $\Delta V$ ), the distance between electrodes ( $d_e$ ), and the thickness of the magnet ( $w_{mag}$ ) on the device's extraction capacity, angular velocity, and gas production. By examining the influence of each parameter on the device's performance, the analysis aims to identify the optimal combination of parameters for maximizing its effectiveness.

To ensure that the MHD drive fits within a 1U volume, a maximum external radius of 5cm is set. To determine the optimal geometry and magnet size for CubeSat propulsion applications, it is necessary to conduct a parametric analysis.

For this study, the proportions  $R_i = 1.5/2.3R_e$  are maintained and a fixed value of 0.25mm for the bubble diameter is set. The parameters  $\Delta V$  and  $d_e$  are fixed at values of 2.8V and 0.01m, respectively. The magnet thickness is set to  $w_{mag} = 3.175mm$  and the height of the MHD drive is 0.0195m, except in studies that require variation in these parameters.

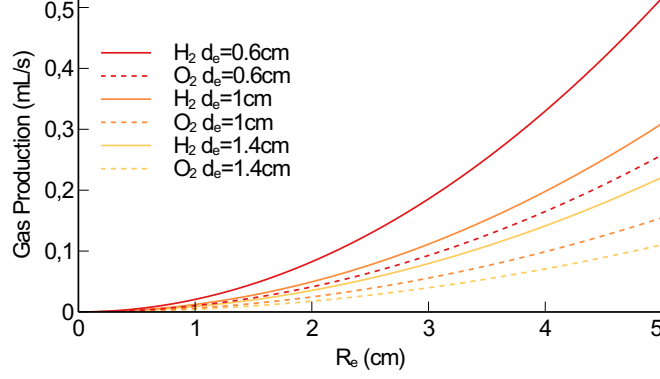


**Fig. 4** Gas production variation with external radius and electrode separation for  $\Delta V = 2.8V$ .

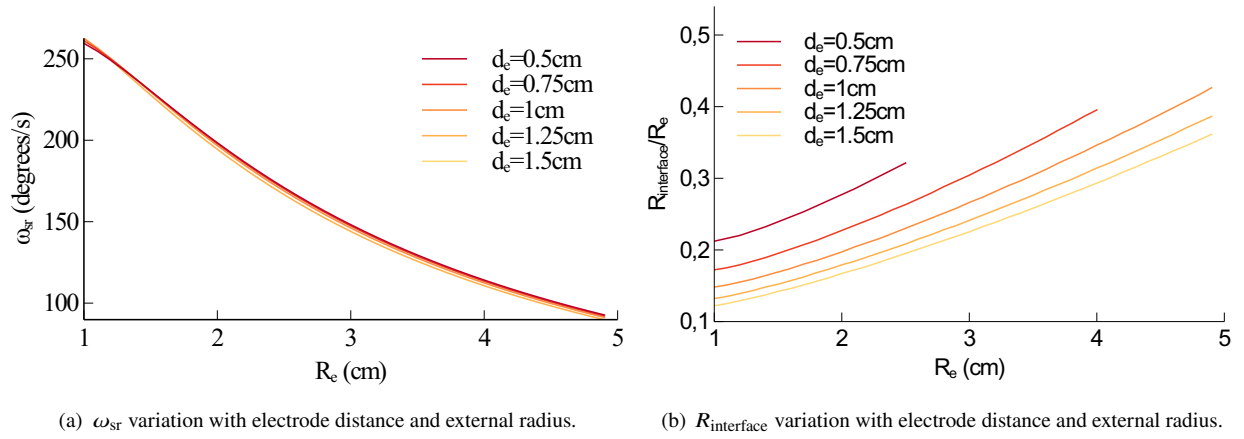


**Fig. 5** Electrode distance parametric study results.

### 1. Gas Production

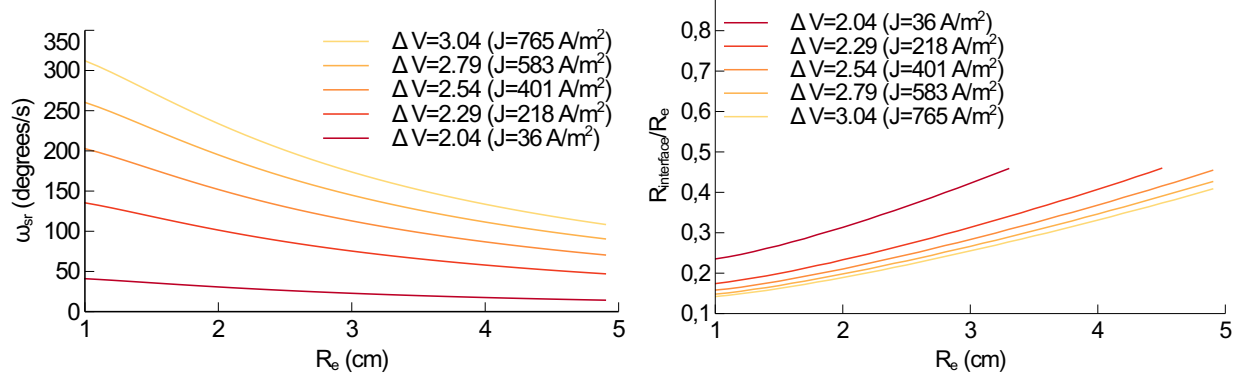
Figure 4 shows the amount of  $H_2$  and  $O_2$  produced for different MHD radius  $R_e$  and electrode's distance  $d_e$ . On one hand, since the electrode surface,  $A$  is directly proportional to the square of  $R_e$ , and the current intensity is also directly related to  $A$  according to Eq. 13, the gas production increases with the square of  $R_e$ , as shown in Fig. 4.

On the other hand, decreasing the distance between electrodes  $d_e$  results in higher current intensity, as indicated by Eq. 13, leading to more gas production, as also shown in Fig. 4.

### 2. Electrode Distance Influence

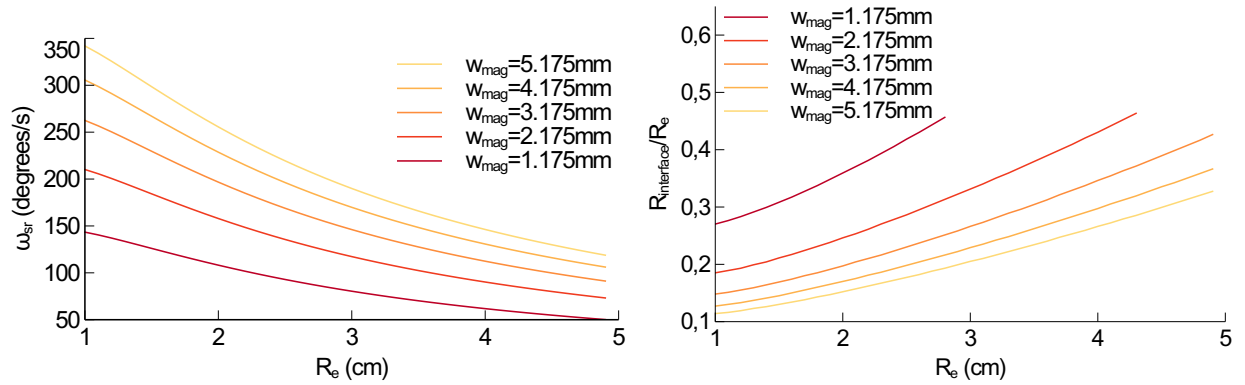
The effect of  $d_e$  on the angular velocity is twofold. A lower value of  $d_e$  leads to higher current intensity according to Eq. 13, resulting in an increase in the Lorentz force. However, this also reduces the volume where the Lorentz force is applied. These opposing effects tend to cancel each other out, as illustrated by the results in Fig 5(a), which show no significant effect of  $d_e$  on the angular velocity.

However, a lower value of  $d_e$  does lead to higher gas production, resulting in a higher interface radius. At the same time, a lower  $d_e$  reduces the surface area available for gas evacuation. If  $d_e$  is too small, the gas produced cannot be evacuated at the same rate that it is produced, and the space between the electrodes is filled with gas, effectively halting the electrolysis process. This effect is illustrated in Fig. 5(b), for small  $d_e$  values, when the  $R_e$  increases and the  $\omega_{sr}$  decreases, the MHD drive cannot evacuate all the gas generated and the electrolysis process is stopped.



(a)  $\omega_{sr}$  variation with potential difference and external radius. (b)  $R_{interface}$  variation with potential difference and external radius.

**Fig. 6 Potential difference parametric study results.**



(a)  $\omega_{sr}$  variation with magnet thickness and external radius. (b)  $R_{interface}$  variation with magnet thickness and external radius.

**Fig. 7 Magnet thickness parametric study results.**

### 3. Potential Difference Influence

The influence of  $\Delta V$  on the MHD drive performance is also studied, with the objective of maximizing gas production and angular velocity. This parameter is ideally fixed at the highest possible value without causing electrolyte decomposition. Figure 6(a) shows that the angular velocity increases with  $\Delta V$ , as a higher value leads to a higher current intensity and a stronger Lorentz Force. Although the higher intensity also results in increased gas production, the increment in angular velocity is sufficient to reduce the interface radius.

However, as observed in  $d_e$  variations, for extremely low values of  $\Delta V$ , the velocity is insufficient to expel the produced gas from the space between electrodes. This can be observed in Fig. 6(b).

### 4. Magnet Thickness Influence

A larger magnet produces a stronger magnetic field, increasing the Lorentz Force and the angular velocity. However, gas production remains constant, resulting in a decrease in interface radius for thicker magnets. Conversely, for thin magnets, the applied Lorentz Force is weaker, resulting in a smaller angular velocity, as shown in Fig. 7(a). If the gas production rate is maintained and the angular velocity is reduced, the extraction capacity decreases, which leads to the space between electrodes filling with gas and the electrolysis process stopping, this is observed for the thinner magnets in Fig. 7(b).



### 5. CubeSat Scalability

The results obtained provide useful insights for designing the geometry of the MHD drive. It is clear from the data that, in order to maximize the performance, the value of  $\Delta V$  should be set at the highest possible level without leading to electrolyte decomposition, which happens around 2.8V (2.909 V for  $KOH \rightarrow K(c)/OH^-$  and 2.704V for  $NaOH \rightarrow Na(c)OH^-$ ) [37].

The  $d_e$  parameter has a significant impact on the MHD performance. A smaller  $d_e$  results in higher gas production while maintaining the angular velocity. However, it also leads to a higher interface radius due to the increased gas production and reduced surface area available for gas evacuation. If the  $d_e$  is reduced beyond a certain critical point, the gas production rate exceeds the evacuation capacity, and the electrolysis process stops. This can cause gas to partially replace the liquid, disrupting the flow of the electrodes and reducing the Lorentz Force, thus decreasing the angular velocity.

Finally, the results show that increasing the magnet thickness significantly improves the performance of the MHD drive without significantly increasing its size. The data presented in Fig. 7 predicts that an increase of just 2mm in the magnet's thickness ( $w_{mag}$ ) leads to an improvement in angular velocity of 30% and a reduction of 23.5% in the interface radius (for every radius).

Taking these factors into consideration, an optimal design can be proposed. The MHD drive should be designed with a maximum radius of 5cm, including the magnet thickness and the external radius. A  $w_{mag}$  of 5.175mm is used, resulting in an external radius of  $R_e = 4.482$ cm. After several iterations, an optimal  $d_e$  of 0.65cm has been found to provide a high gas production rate without preventing gas evacuation. These design parameters lead to an angular velocity of 132.4 degrees/s,  $H_2$  production rate of 0.382 mL/s,  $O_2$  production rate of 0.191 mL/s, and an interface radius of 1.63cm, which is 36.43% of the external radius. The gas produced by this design would allow to fill the combustion chamber of the Cislunar Explorers [8] in 7 min approximately, assuming that this deposit has dimensions of 1Ux0.5Ux0.5U. The proposed MHD drive design, without considering the additional weight of water, would have a mass of 0.15kg approximately.

## IV. Conclusions

The preliminary analytical results obtained using a first-order approach to balance the Lorentz moment and the shear stress moment predicted the angular velocity of the electrolyte. The model's accuracy is dependent on the geometry, the magnetic field, and the current intensity. For a given geometry the model shows a proportional relationship between the angular velocity and the Lorentz force, where  $\omega_{sr} \propto F_{Lorentz}^{2/3}$ .

A parametric analysis showed that gas production increases with larger  $R_e$ , lower  $d_e$ , and higher  $\Delta V$ . However,  $R_e$  and  $\Delta V$  shall be limit to 5 cm and 2.8 V, respectively, to avoid exceeding 1 U and causing electrolyte decomposition. As for the angular velocity, increasing both  $\Delta V$  and magnet thickness  $w_{mag}$  leads to a higher Lorentz force and, consequently, higher angular velocity. However, variation in  $d_e$  has no effect on the angular velocity, as it has two opposing effects that cancel each other out, i.e., a lower  $d_e$  increases the current intensity, while at the same time reducing the volume where the Lorentz Force is applied. Regarding the extraction capacity, for every case, there is a critical point where the gas produced cannot be evacuated from the space between electrodes due to high gas production, low angular velocity, small  $d_e$ , or a combination of these factors. The extraction capacity improves with higher  $\Delta V$  and magnet size but worsens for lower  $d_e$ . A proposed MHD design to maximize gas production and avoid MHD drive failure due to evacuation problems would consist of an external radius of 4.48 cm,  $w_{mag} = 5.175$  mm, an applied voltage difference of 2.8 V, and a  $d_e = 0.65$  cm. The developed model predicts an angular velocity of 132.4 degrees/s, a gas production rate for  $H_2$  of 0.382 mL/s, a  $O_2$  production rate of 0.191 mL/s, and an interface radius of 1.63cm which is 36.43% of the external radius  $R_e$ . This design would have a mass of 0.15kg and according to the developed model would allow to fill the Cislunar Explorer's [8] combustion chamber within 7 min.

Based on the analytical results, the design of the MHD drive as a tool for phase separation in microgravity has the potential to be successful. The predicted angular velocity, the terminal velocity of the bubbles, and the gas extraction capacity demonstrate that the proposed MHD drive could effectively separate the liquid and gas phases. The compact size of the MHD drive, as described in the proposed geometry, makes it a suitable option for CubeSat propulsion.

## Acknowledgments

This work was supported by the Georgia Space Grant Consortium and by the PROMOE Santander International Mobility Program of the Polytechnical University of Valencia.

## References

- [1] SLO, C. P., "CubeSat Design Specification Rev.13," Tech. rep., California Polytechnic State University, 2014. URL [https://static1.squarespace.com/static/5418c831e4b0fa4ecac1bacd/t/56e9b62337013b6c063a655a/1458157095454/cds\\_rev13\\_final2.pdf](https://static1.squarespace.com/static/5418c831e4b0fa4ecac1bacd/t/56e9b62337013b6c063a655a/1458157095454/cds_rev13_final2.pdf).
- [2] Bouwmeester, J., and Guo, J., "Survey of worldwide pico- and nanosatellite missions, distributions and subsystem technology," *Acta Astronautica*, Vol. 67, No. 7, 2010, pp. 854–862. <https://doi.org/https://doi.org/10.1016/j.actaastro.2010.06.004>.
- [3] Nayyar, S., Kumar, S., and Suhag, V., "Earthquake Signature Detection Using Cubesat Technology," *Journal of Advance Research in Electrical and Electronics Engineering*, Vol. 1, No. 2, 2014, pp. 04–06. <https://doi.org/https://doi.org/10.53555/nneee.v1i2.256>.
- [4] Evans, D., and Merri, M., "OPS-SAT: A ESA nanosatellite for accelerating innovation in satellite control," *SpaceOps 2014 Conference*, Pasadena, CA, 2014. <https://doi.org/10.2514/6.2014-1702>, AIAA Paper 2014-1702.
- [5] Kitts, C., Ronzano, K., Rasay, R., Mas, I., Williams, P., Mahacek, P., Minelli, G., Hines, J., Agasid, E., Friedericks, C., et al., "Flight results from the GeneSat-1 biological microsatellite mission," *21st Annual AIAA/USU Conference on Small Satellites*, Santa Clara, CA, 2007. URL <https://digitalcommons.usu.edu/cgi/viewcontent.cgi?article=1502&context=smallsat>.
- [6] Schoolcraft, J., Klesh, A., and Werne, T., "MarCO: interplanetary mission development on a CubeSat scale," *Space Operations: Contributions from the Global Community*, 2017, pp. 221–231. <https://doi.org/10.2514/6.2016-2491>.
- [7] "4 - Interplanetary CubeSat missions," *Cubesat Handbook*, edited by C. Cappelletti, S. Battistini, and B. K. Malphrus, Academic Press, 2021, pp. 85–121. <https://doi.org/https://doi.org/10.1016/B978-0-12-817884-3.00004-7>.
- [8] Zucherman, A., Jawork, K., Buchwald, A., Naikawadi, A., Robinson, C., Kumar, E., Kann, E., Orellana, G., Zakoworotny, M., Alon, O., et al., "Cislunar Explorers: Lessons Learned from the Development of an Interplanetary CubeSat," *34th AIAA/USU Conference on Small Satellites*, Logan, UT, 2020. URL <https://digitalcommons.usu.edu/smallsat/2020/all2020/92/>.
- [9] Prejean, T., "NanoRacks CubeSat Deployer," Tech. Rep. NR-NRCSD-S0003, NanoRacks, 2018. URL <https://nanoracks.com/wp-content/uploads/Nanoracks-CubeSat-Deployer-NRCSD-IDD.pdf>.
- [10] John, F., Jeff, K., Corey, C., Patel, K., and Orbit, B. P. V., "LauncherOne Now in Orbit: Dedicated Air-Launch Brings Proven, Responsive Space," Tech. Rep. SSC21-IV-05, VirginOrbit, 2021. URL <https://digitalcommons.usu.edu/cgi/viewcontent.cgi?article=5034&context=smallsat>.
- [11] Sarda, K., Grant, C., Eagleson, S., Kekez, D. D., and Zee, R. E., "Canadian Advanced Nanospace Experiment 2: Om-Orbit Experience with an Innovative Three-Kilogram Satellite," *4S Symposium Small Satellites Systems and Services*, ESA Special Publication, Noordwijk, Netherlands: European Space Agency, Vol. 660, edited by L. Conroy, 2008, p. 62. URL <https://ui.adsabs.harvard.edu/abs/2008ESASP.660E..62S>.
- [12] Manzoni, G., and Brama, Y. L., "Cubesat Micropropulsion Characterization in Low Earth Orbit," *Proceedings of the 29th AIAA/USU Conference Small Satell*, Logan, UT, 2015. URL <https://digitalcommons.usu.edu/smallsat/2015/all2015/26/SSC15-IV-5>.
- [13] Hejmanowski, N., Woodruff, C., Burton, R., Carroll, D., and Palla, A., "CubeSat High Impulse Propulsion System (CHIPS) Design and Performance," *Proceedings of 63rd JANNAF Propulsion Meeting (8th Spacecraft Propulsion)*, Phoenix, AZ, 2016, p. 1. URL [https://www.researchgate.net/profile/David-Carroll-13/publication/323225650\\_CubeSat\\_High\\_Impulse\\_Propulsion\\_System\\_CHIPS\\_Design\\_and\\_Performance/links/5a86f4010f7e9b1a954c854e/CubeSat-High-Impulse-Propulsion-System-CHIPS-Design-and-Performance.pdf](https://www.researchgate.net/profile/David-Carroll-13/publication/323225650_CubeSat_High_Impulse_Propulsion_System_CHIPS_Design_and_Performance/links/5a86f4010f7e9b1a954c854e/CubeSat-High-Impulse-Propulsion-System-CHIPS-Design-and-Performance.pdf).
- [14] Coletti, M., Guarducci, F., and Gabriel, S., "A micro PPT for Cubesat application: Design and preliminary experimental results," *Acta Astronautica*, Vol. 69, No. 3, 2011, pp. 200–208. <https://doi.org/https://doi.org/10.1016/j.actaastro.2011.03.008>.
- [15] Alhorn, D., "NanoSail-D: The Small Satellite That Could!" Tech. Rep. SSC11-VI-1, AIAA/USU Conference Small Satell, Technical Session VI: Small but Mighty, 2011. URL <https://digitalcommons.usu.edu/smallsat/2011/all2011/37/>.
- [16] van Paridon, A., and Petro, E., "Survey of water powered propulsion systems," *AIAA Propulsion and Energy 2021 Forum*, AIAA Paper 2021-3566, 2021. <https://doi.org/https://doi.org/10.2514/6.2021-3566>.
- [17] Doyle, K. P., and Peck, M. A., "Water Electrolysis Propulsion as a Case Study in Resource-Based Spacecraft Architecture (February 2020)," *IEEE Aerospace and Electronic Systems Magazine*, Vol. 34, No. 9, 2019, pp. 4–19. <https://doi.org/10.1109/MAES.2019.2923312>.

- [18] “ARO Aurora Resistojet One Datasheet,” 2020. URL <https://aurorapt.fi/downloads/ARO.pdf>.
- [19] Nogawa, Y., and Tahara, H., “Evolutional Electrical Propulsion with Water Propellant DC Arcjet,” *35th International Electric Propulsion Conference*, Atlanta, GA, 2017, pp. 2017–413. URL [http://electricrocket.org/IEPC/IEPC\\_2017\\_413.pdf](http://electricrocket.org/IEPC/IEPC_2017_413.pdf).
- [20] Koizumi, H., Asakawa, J., Nakagawa, Y., Nishii, K., Takao, Y., Nakano, M., and Funase, R., “Assessment of Micropropulsion System Unifying Water Ion Thrusters and Water Resistojet Thrusters,” *Journal of Spacecraft and Rockets*, Vol. 56, No. 5, 2019, pp. 1400–1408. <https://doi.org/10.2514/1.A34407>.
- [21] Kirtley, D., Pancotti, A., Slough, J., and Pihl, C., “Steady Operation of an FRC Thruster on Martian Atmosphere and Liquid Water Propellants,” *48th AIAA/ASME/SAE/ASEE Joint Propulsion Conference*, 2012. <https://doi.org/10.2514/6.2012-4071>, AIAA Paper 2012-4071.
- [22] Schwertheim, A., and Knoll, A., “The water electrolysis hall effect thruster (wet-het): Paving the way to dual mode chemical-electric water propulsion,” *36th International electric propulsion conference*, Vienna, Austria, 2019, p. 259. URL <http://electricrocket.org/2019/259.pdf>.
- [23] Rabade, S., Barba, N., Garvie, L., and Thangavelautham, J., “The case for solar thermal steam propulsion system for interplanetary travel: Enabling simplified ISRU utilizing NEOs and small bodies,” *Proceedings of the 67th International Astronautical Congress*, Guadalajara, Mexico, 2016. URL [https://asteroid.arizona.edu/iac2016\\_steam\\_propulsion.pdf](https://asteroid.arizona.edu/iac2016_steam_propulsion.pdf).
- [24] Sutton, G., and Biblarz, O., *Rocket Propulsion Elements*, Wiley, Hoboken, New Jersey, 2001.
- [25] Erickson, R. J., Howe, J., Kulp, G. W., and Van Keuren, S. P., “International space station united states orbital segment oxygen generation system on-orbit operational experience,” *SAE International Journal of Aerospace*, Vol. 1, No. 2008-01-1962, 2008, pp. 15–24. <https://doi.org/https://doi.org/10.4271/2008-01-1962>.
- [26] Tilton, D. E., and Tilton, C. L., “Entrained droplet separator,” 1994. US Patent 5314529.
- [27] Sakurai, M., Shima, A., Sone, Y., Ohnishi, M., Tachihara, S., and Ito, T., “Air Revitalization Development of Oxygen Generation Demonstration on JEM (KIBO) for Manned Space Exploration,” *44th International Conference on Environmental Systems*, Tucson, Arizona, 2014, pp. 1–7. URL <http://hdl.handle.net/2346/59644>.
- [28] Weislogel, M. M., Thomas, E. A., and Graf, J. C., “A Novel Device Addressing Design Challenges for Passive Fluid Phase Separations Aboard Spacecraft,” *Microgravity Science and Technology*, Vol. 21, No. 3, 2008, p. 257. <https://doi.org/10.1007/s12217-008-9091-7>.
- [29] Romero-Calvo, A., Schaub, H., and Cano-Gómez, G., “Diamagnetically Enhanced Electrolysis and Phase Separation in Low Gravity,” *Journal of Spacecraft and Rockets*, Vol. 59, No. 1, 2022, pp. 59–72. <https://doi.org/10.2514/1.A35021>.
- [30] Romero-Calvo, Á., Akay, Ö., Schaub, H., and Brinkert, K., “Magnetic phase separation in microgravity,” *npj Microgravity*, Vol. 8, No. 1, 2022, p. 32. <https://doi.org/10.1038/s41526-022-00212-9>.
- [31] Heywood, J. B., *Internal combustion engine fundamentals*, McGraw-Hill Education, New York City, 2018.
- [32] Schlichting, H., and Kestin, J., *Boundary layer theory*, Vol. 121, Springer, Midtown Manhattan, New York City, 1961.
- [33] Munson, B. R., Okiishi, T. H., Huebsch, W. W., and Rothmayer, A. P., *Fluid mechanics*, Wiley Singapore, 2013.
- [34] Day, M. A., “The no-slip condition of fluid dynamics,” *Erkenntnis*, Vol. 33, No. 3, 1990, pp. 285–296. <https://doi.org/https://doi.org/10.1007/BF00717588>.
- [35] Hibbeler, R., *Mechanics of Materials*, Pearson Education, New Jersey USA, 2004.
- [36] Griffiths, D. J., *Introduction to electrodynamics*, Pearson Cambridge University Press, Cambridge, England, 2017. <https://doi.org/10.1017/9781108333511>.
- [37] Bratsch, S. G., “Standard electrode potentials and temperature coefficients in water at 298.15 K,” *Journal of Physical and Chemical Reference Data*, Vol. 18, No. 1, 1989, pp. 1–21. <https://doi.org/https://doi.org/10.1063/1.555839>.
- [38] Clift, R., Grace, J. R., and Weber, M. E., “Bubbles, drops, and particles,” 2005.
- [39] Liu, L., Yan, H., Zhao, G., and Zhuang, J., “Experimental studies on the terminal velocity of air bubbles in water and glycerol aqueous solution,” *Experimental Thermal and Fluid Science*, Vol. 78, 2016, pp. 254–265. <https://doi.org/https://doi.org/10.1016/j.expthermflusci.2016.06.011>.
- [40] Romero-Calvo, , Herrada, M., Cano-Gómez, G., and Schaub, H., “Fully coupled interface-tracking model for axisymmetric ferrohydrodynamic flows,” *Applied Mathematical Modelling*, Vol. 111, 2022, pp. 836–861. <https://doi.org/https://doi.org/10.1016/j.apm.2022.06.046>.